Engineering Structures 169 (2018) 94–106

Contents lists available at ScienceDirect

Engineering Structures

journal homepage: www.elsevier.com/locate/engstruct

Numerical evaluation of ductility and energy absorption of steel rings constructed from plates

Zahra Andalib[a], Mohammad Ali Kafi[b], Mohammad Bazzaz[a,*], Seyedbabak Momenzadeh[c]

[a] Department of Civil, Environmental, and Architectural Engineering, University of Kansas, Lawrence, KS 66045, USA
[b] Faculty of Civil Engineering, Semnan University, P.O. Box: 19111-35131, Semnan, Iran
[c] Thornton Tomasetti, San Francisco, CA 94108, USA

ARTICLE INFO

Keywords:
Ductility
Energy absorption
Steel ring
Steel braces

ABSTRACT

Several studies have been performed to increase the ductility of concentric braces in the past decades. Incorporating an energy-dissipator member in the braces is one of the novel approaches to increase the ductility of the braces. Experimental and numerical studies have shown that steel rings made of steel pipes can be an effective energy-dissipator in the braces. However, due to the limitations on the size of the steel pipes, it is not always possible to find an appropriate pipe to be used in the braces. In the current study, performance of the steel ring made of two half-steel rings is investigated. In addition, effect of the welding or utilizing bolts, thickness of the ring, and material properties on the ductility and energy absorption of the braces is evaluated. Results indicated to the appropriate ductility and energy absorption of made-up steel rings.

1. Introduction

Several unexpected issues were observed in the rigid connections of special moment frames after the Northridge earthquake in 1994. Extensive studies were performed to develop new connections that undergo significant inelastic behavior; such as reduced beam section (RBS) [1,2] and reduced web section (RWS) [3–5] connections. However, stringent design criteria of these connections made the engineering society hesitant to widely use these systems [6]. Braced frames are another type of lateral load resisting systems that became more popular after 1994. In this system, earthquake energy is dissipated through inelastic behavior of the braces. However, premature fracture of the concentric braces of this system in the previous earthquakes has risen doubts about using this member [7] and strict limitations on utilizing these braces are implemented in the design codes [8]. Extensive investigations have been performed with the purpose of increasing the ductility of the braces and several approaches are proposed to avoid the premature fracture in the braces [9–24]. Among the proposed methods, utilizing flexural energy-dissipating fuses is one of the most effective methods to date [25–27]. In this approach, a steel ring can be used in the braces adjacent to the gusset plate connection. Flexural inelastic behavior in the braces due to the steel ring added to the end of the brace leads to significant energy dissipation during an earthquake. Numerous experimental and numerical studies have been done on utilizing steel rings made of steel pipes. It is observed that adding the steel ring to the end of the steel braces results in stable hysteretic behavior of the braces [28–30] and after earthquake, replacing the steel rings is simple and not expensive. Experimental studies have shown that the majority of the damage occurs in the steel ring and other portion of the brace remains elastic. Due to the limitation on the steel pipe size, numerical study on the behavior of steel rings consist of two half-rings formed by rolling of steel plates has been presented in this article. Variety of material and size of steel plates allows the preparation of various steel rings with different capacities. In this paper, numerical study on the performance of three steel rings made up of two half-rings are presented. Previous studies showed the seismic performance of bracing will affect by the connection details [31], so the effect of the steel ring connection to the gusset plate, thickness of the steel rings, and material properties on the behavior of the steel rings is investigated.

2. Literature review

One of the most important features of a lateral load resisting system is possessing an appropriate stiffness, strength, and capability of energy dissipation, simultaneously [32–35]. On the other hand, it is not economically justifiable to design a structure to remain elastic under a moderate earthquake [36–38]. Therefore, based on current seismic

* Corresponding author.
E-mail addresses: Zahra.Andalib@ku.edu (Z. Andalib), mkafi@semnan.ac.ir (M. Ali Kafi), Mohammad.Bazzaz@ku.edu (M. Bazzaz), Smomenzadeh@thorntontomasetti.com (S. Momenzadeh).

https://doi.org/10.1016/j.engstruct.2018.05.034
Received 25 September 2017; Received in revised form 7 May 2018; Accepted 11 May 2018
0141-0296/

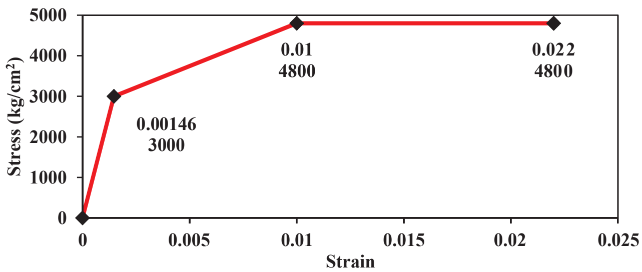

Fig. 1. Stress-strain diagram defined in the software for CT20 Steel.

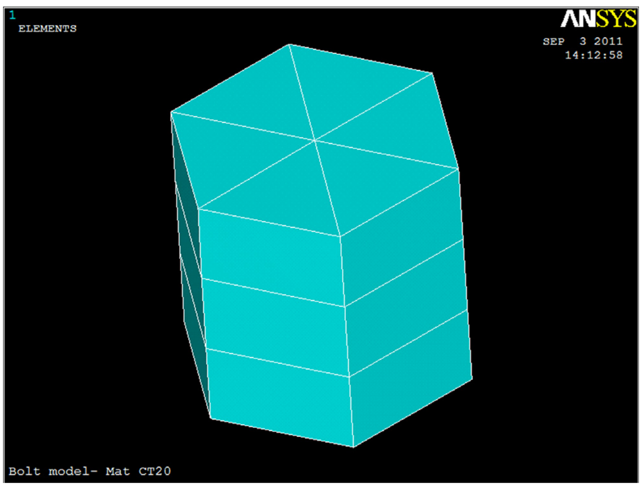

Fig. 2. Bolt modeling using ANSYS.

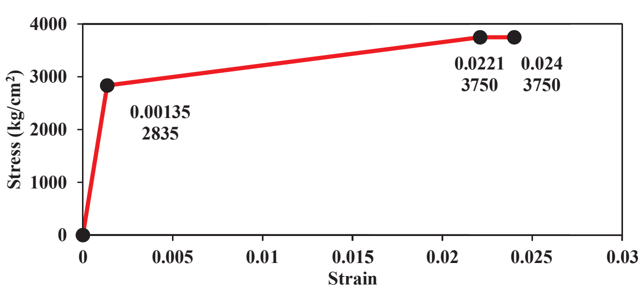

Fig. 3. Stress-strain diagram defined in the software for ST37 Steel.

design approach, it is important that structure experiences an inelastic behavior to dissipate earthquake energy [39–46]. Y-shaped braces are one of the bracing configurations that can be used to resist seismic loads [47,48]. Experimental and numerical studies have been performed on the Y-shaped braces' various buckling modes, such as elastic, inelastic, and out of plane buckling [49,50]. Numerous novel methods have been developed to have a seismic resistant design [29,30,51,52]. Using a passive control system in the structures is among the recently developed methods. In this method, an energy-dissipator member is utilized in the structure to absorb the damages to the structure and to prevent the failure of other members [53,54]. Using hyperelastic material, in a toggle bracing systems is one of these methods [7,55,56].

In the present study, performance of steel ring as an energy dissipator member is investigated. Abbasnia et al. performed an experimental and numerical study on the behavior of the steel rings used in diagonal braces [57]. It was observed that steel rings can effectively improve the behavior of the braces [57]. Steel rings also are innovatively utilized in the off-center braces and their performance are assessed in terms of ductility and energy dissipation [55,57–68].

In the previous studies, a seamless Mannesmann pipe was used as the steel ring. However, dimension and thickness variety of these pipes are limited and it hinders widely usage of this system [55,57–68]. Moreover, pipe installation may not be applicable by ordinary contractors in construction industry [69–71]. In the current article, the steel pipe is replaced with two half-rings and a connecting plate between them to solve the aforementioned issues. Three different models with various connections are simulated in ANSYS to study the effect of the steel ring connection on their performance. In addition, influence of material properties and half-ring' thickness is also evaluated.

3. Modeling

In the first step, based on the experimental results, steel material properties were defined in the ANSYS software. Fig. 1 presents the CT20 steel stress-strain diagram defined in the software. Solid 45, Contact 174, and Target 170 three dimensional elements were used in the simulation and solid elements were employed to model the bolts. Surface to surface Contact 174 elements were used to connect plates and bolts as shown in Fig. 2. In order to model weld, nods were merged together at the location of weld beads. Fig. 3 presents the ST37 steel stress-strain diagram. Steel rings and connection plates were merged together, and simulation of weld is neglected in the current study assuming that failure does not occur in the welds. Surface-to-surface contact was defined between the connection plate and steel rings to simulate the actual behavior of the steel ring. Fixed boundary condition was applied to one end of the model while an axial force was applied to the other end to investigate the behavior of the model. A mesh size of 7 mm was utilized in the finite element simulation and a total number of 3556 and 3120 elements were used in bolted and welded models, respectively. Table 1 summarizes simulated models specifications. The phrase "ST37/CT20" indicates the type of steel used. The expression "TH12/TH20" is an abbreviation for the thickness of a 12 mm half-ring or 20 mm half-ring, "P" means pin connectors and use for models with bolts, and "SW" stands for semi-weld. Figs. 4 and 5 show the Schematic details of models used in ANSYS, which are respectively called ST37-TH12-SW and CT20-TH12-P for brevity. Figs. 4 and 5 present schematic details of model ST37-TH12-SW and CT20-TH12-P, respectively.

4. Geometrical specification of the ring

The relationships between strength of material, variation of the ring diameter, and its internal forces in the elastic zone under load P are shown in Fig. 6. Moreover, Eqs. (1-7) represent the same concept. According to Castigliano's second theorem [72], $\delta_y = \partial U/\partial V$, $\delta_x = \partial U/\partial H$,

Table 1
Details of the simulated models.

Model type	Steel type	Outer diameter (mm)	Thickness (mm)	Length (mm)	Connection plates length (mm)	Connection plates width (mm)	Connection plates thickness (mm)	Connector type (mm)
CT20-TH12-C	CT20	220	12	100	220	170	12	7 Fillet
CT20-TH12-P								Bolts
CT20-TH12-SW								7 Fillet
ST37-TH12-SW	ST37							
ST37-TH20-SW			20					

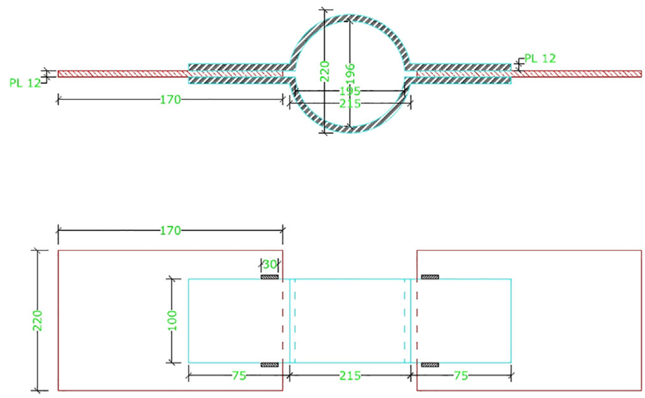

Fig. 4. Schematic details of model ST37-TH12-SW (units are in mm).

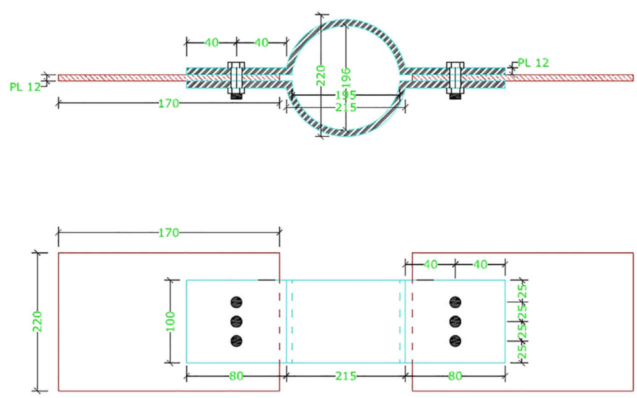

Fig. 5. Schematic details of model CT20-TH12-P (units are in mm).

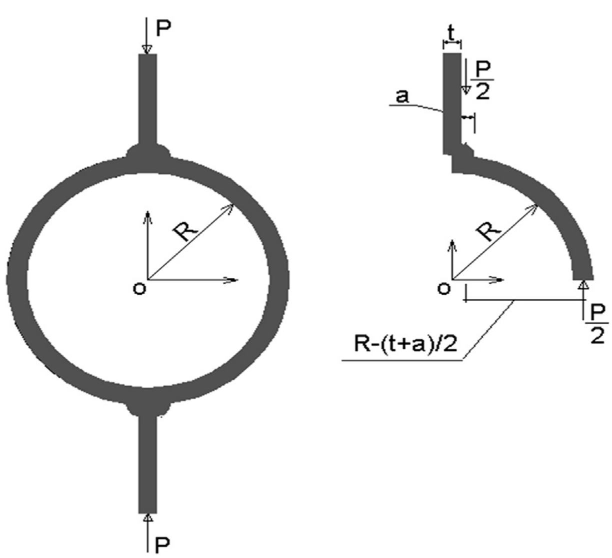

Fig. 6. Schematic of the ring.

and $\theta = \partial U/\partial M_0$, where U is complementary energy of flexure, V is vertical force, H is horizontal force, θ is rotation of the upper end, and M_0 is a couple [73]:

$$M^{+} = 0.3183PR \quad \theta = \frac{\pi}{2} \tag{1}$$

$$M^{-} = 0.1817PR \quad \theta = 0 \tag{2}$$

$$I = \frac{1}{12}t^3L \tag{3}$$

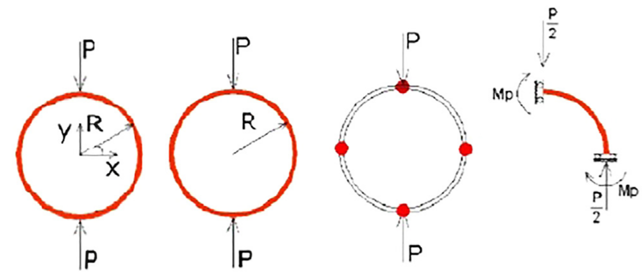

Fig. 7. Plastic hinge formation.

$$\delta_y = -0.149\frac{PR^3}{EI} \tag{4}$$

$$\delta_x = +0.137\frac{PR^3}{EI} \tag{5}$$

$$T = \frac{1}{2}P\cos\theta \tag{6}$$

$$V = -\frac{1}{2}P\sin\theta \tag{7}$$

There are four plastic hinges as shown in Fig. 7 by increasing the load. Also, the balance relationship in the plastic limit state can be illustrated as Eqs. (810):

$$2M_P = \frac{PR}{2} \Rightarrow P = \frac{4M_P}{R} \tag{8}$$

$$M_P = \frac{t^2L\sigma_y}{4} \tag{9}$$

$$P = \frac{t^2L\sigma_y}{R} \tag{10}$$

where:

M^{+}, M^{-}: Bending moment in the ring at $\theta = \frac{\pi}{2}$ and $\theta = 0$, respectively.
I: Moment of inertia of the ring section
t: Thickness of the ring
l: Width of the ring
δ_x, $\delta_{y:}$ Horizontal and vertical displacement of the ring's end, respectively.
P: Axial load
R: Ring radius
E: Modulus of elasticity
T, V: Axial and shear force in the ring, respectively.
M_P: Plastic moment of the section
σ_y: Axial stress in the ring in y direction.

As observed, the bearing load capacity of the ring is directly correlated with its length, yielding stress, and ring thickness squared. Also, it is inversely correlated with its radius. According to achieved bearing capacity of steel ring, a ring is considered with external diameter of 220 mm and thickness of 12 mm.

5. Cyclic loading

A cyclic loading calculated based on ATC 24 [74] was applied to the model. A displacement control loading calculated based on the yielding displacement of the model is used to in the current study. Fig. 8 presents the loading sequence applied to the model, where δ_i is the maximum displacement at the i^{th} cycle of loading history; n_i is the number of cycles with the peak of δ_i; and Δ is yielding displacement of the damper. Fig. 9 shows loading and boundary condition nods. It should be mention that all degrees of freedom are restrained on support nods.

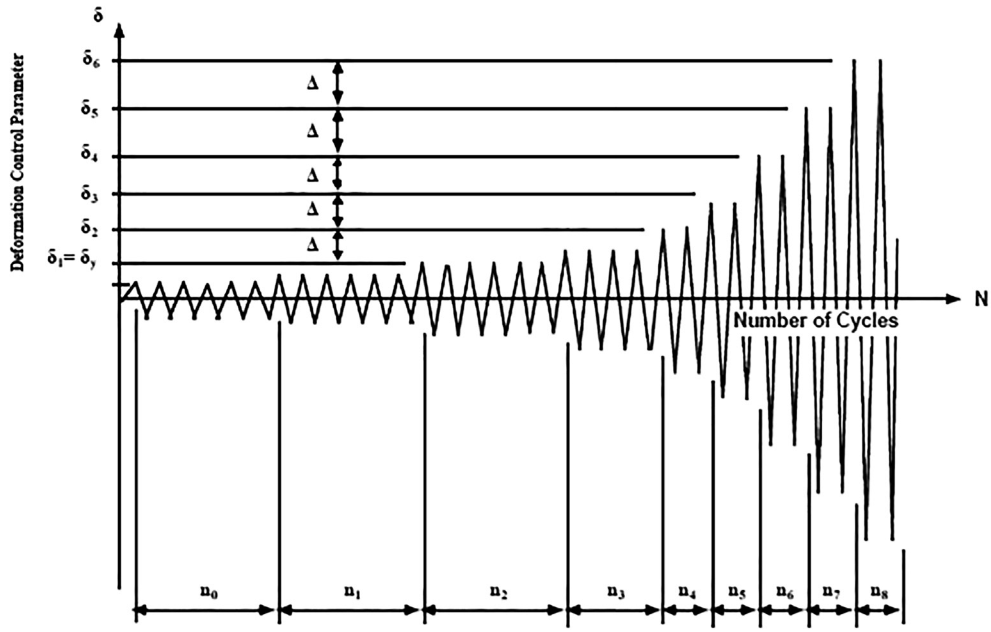

Fig. 8. Loading history in ATC 24 code [74].

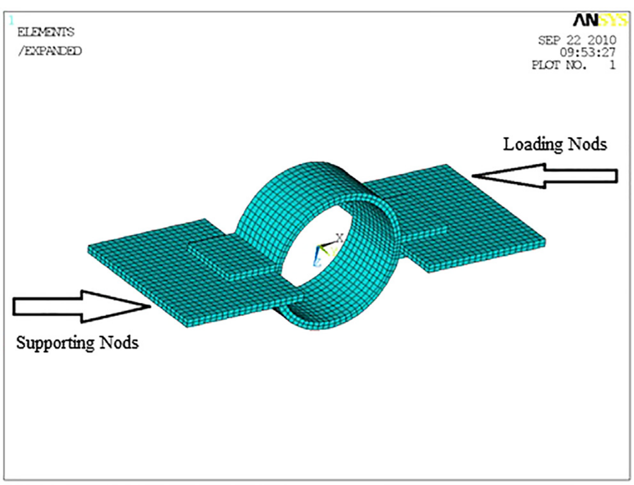

Fig. 9. Loading and supporting nods in ANSYS for CT20_TH12_C model.

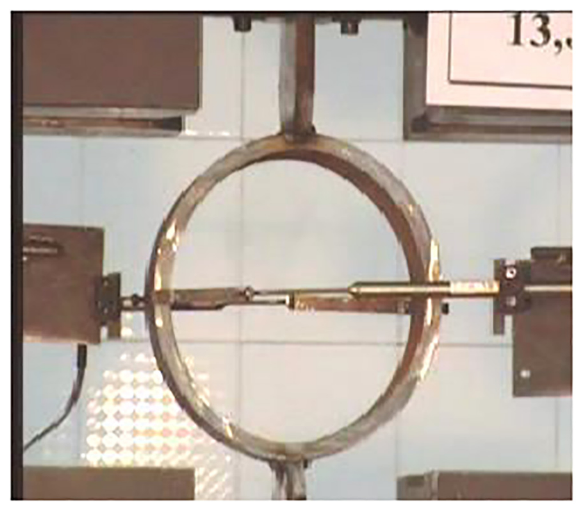

Fig. 10. Tested specimen by Abbasnia [57].

6. Modeling verification

An experimental test performed by Abbasnia et al. in 2008 [57] was used to verify the accuracy of the simulation. The specimen consisted of a steel ring with outer diameter of 220 mm, thickness of 12 mm, and a length of 100 mm. Two 200 × 170 × 12 mm^3 connection plates were also connected to the steel ring with a 7 mm fillet weld. Fig. 10 presents the tested specimen and Fig. 11 shows the ANSYS simulation for CT20_TH12_C model.

Load displacement result of the simulated ring under cyclic loading presented in Fig. 8 is shown in Fig. 12. Model was pushed until the peak strain in the model reaches the ultimate strain. Two linearizations have been performed by FEMA 356 proposed method [75]. The maximum vertical displacement and corresponding vertical displacement of the system at the end of the tensile elastic limit are 20.16 mm and 2.79 mm, respectively. On the other hand, the aforementioned parameters under the compression force were 19.93 mm and 3.09 mm, respectively. Therefore, the ductility of the model can be calculated, such that:

$$\mu = \frac{\Delta_{Max}}{\Delta_y} = \frac{20.16}{2.79} = 7.23 \quad \text{Tension} \tag{11}$$

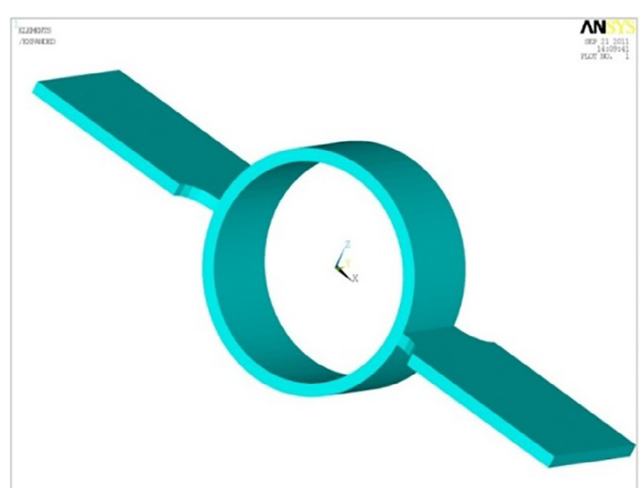

Fig. 11. Simulated steel ring using ANSYS for CT20_TH12_C model.

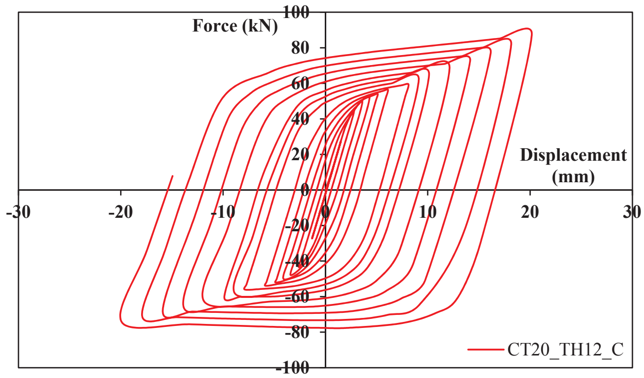

Fig. 12. Force-vertical displacement plot for simulated ring.

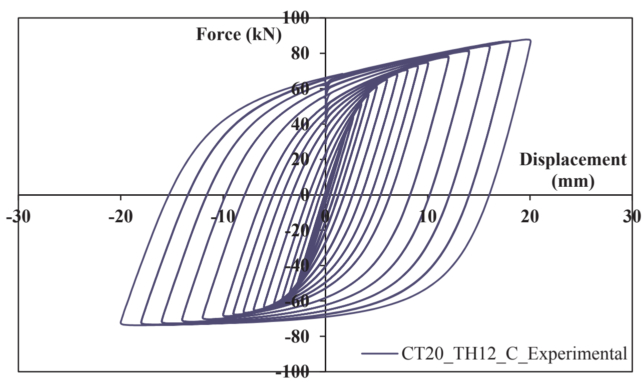

Fig. 13. Force-vertical displacement plot for tested specimen [57].

$$\mu = \frac{\Delta_{Max}}{\Delta_y} = \frac{19.93}{3.09} = 6.45 \quad \text{Compression} \tag{12}$$

In addition, Fig. 13 presents the hysteretic behavior of the tested specimen [57]. The maximum tension and compression force sustained by the model was 87.74 kN and 73.39 kN, respectively, and the peak displacement was around 19.92 mm and 20.00, respectively.

Comparison between the numerical model and experimental test, provided in Fig. 14, demonstrated the fact that simulation can successfully predict the behavior of the tested steel ring and results are in good agreement. Fig. 15 shows Von Misses stress under cyclic load for CT20_TH12_C in ANSYS. It can be observed that stress is mainly concentrated at two ends of the ring and stress intensity in the other portions of the ring is relatively low.

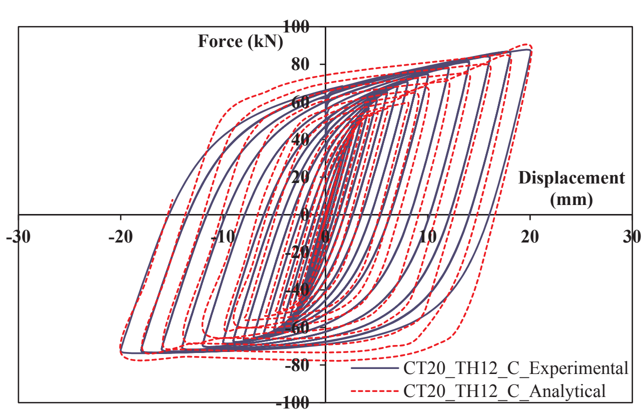

Fig. 14. Comparative hysteresis plots for simulation and test results.

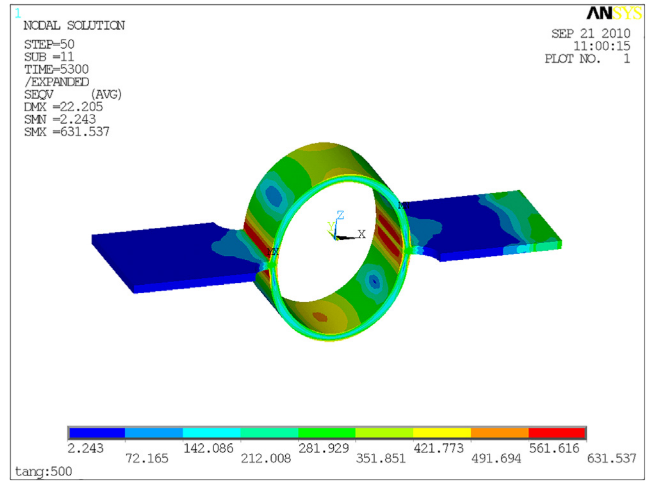

Fig. 15. Von Misses stress under cyclic load for CT20_TH12_C model.

7. Numerical model

7.1. Steel ring made of 12 mm plate and bolts with CT20 steel

The model that had been used in the previous section was simulated again while the steel ring was replaced with two half-rings with outer diameter of 220 mm and thickness of 12 mm. The half-rings were connected to each other with bolts. Ductility and energy dissipation of the model is evaluated in this section. The model was names CT20-TH12-P representing the CT20 material properties, 12 mm thickness, and bolts as the connector of the half-rings. Load displacement diagram of the model is presented in Fig. 16. Similar to the tested specimen, the model was pushed until the peak strain reached the ultimate strain. The maximum tension and compression forces were 108.3 kN and 83.57 kN, respectively.

Envelope of the hysteretic response of the steel ring is presented in Fig. 17. As can be seen in this figure, the maximum vertical displacement and corresponding vertical displacement of the system at the end of the tensile elastic limit are 30.29 mm and 2.89 mm, respectively, based on two linearizations method of FEMA 356 [75]. Similarly, the aforementioned parameters under the compression force were 30.25 mm and 3.10 mm, respectively. Therefore, the ductility of the model can be calculated, such that:

$$\mu = \frac{\Delta_{Max}}{\Delta_y} = \frac{30.29}{2.89} = 10.5 \quad \text{Tension} \tag{13}$$

$$\mu = \frac{\Delta_{Max}}{\Delta_y} = \frac{30.25}{3.10} = 9.75 \quad \text{Compression} \tag{14}$$

Figs. 18 and 19 present the energy vs. cycle and load vs. cycle of the steel ring, respectively. It can be observed that the inelastic capacity of

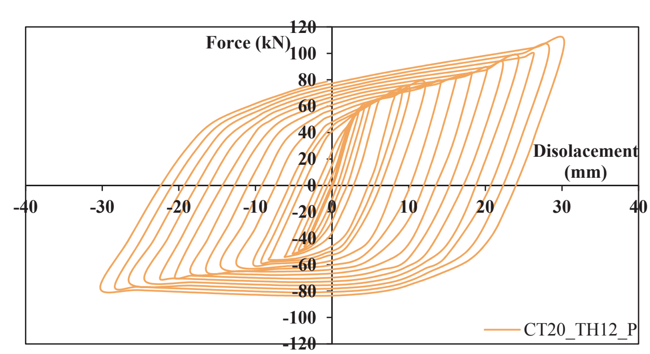

Fig. 16. Force-vertical displacement plot for CT20-TH12-P model.

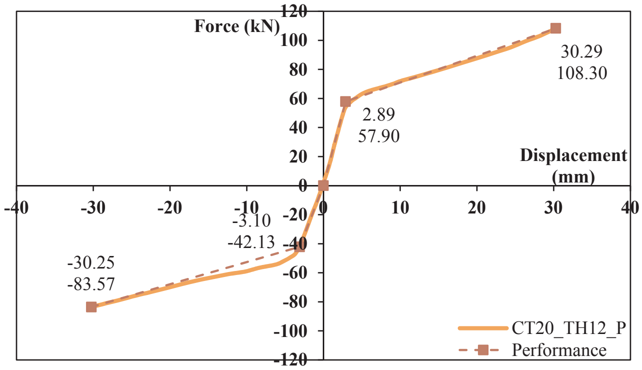

Fig. 17. Hysteresis loop push of force-displacement plot for CT20-TH12-P model.

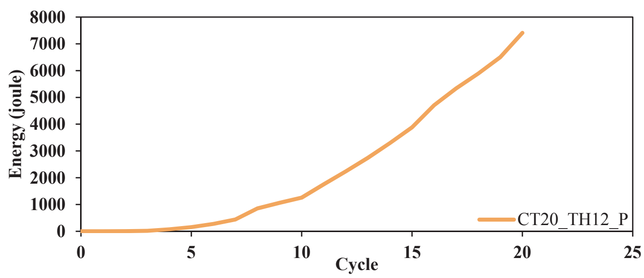

Fig. 18. Energy-loading cycle plot for CT20-TH12-P model.

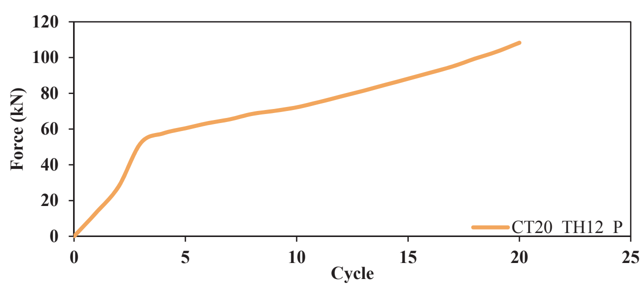

Fig. 19. Force-loading cycle plot for CT20-TH12-P model.

the ring is 1.87 times of its elastic capacity. It can also be seen that energy in the last cycle is about 97 times of the one in the last cycle of the elastic range. In other words, energy absorption/force in the last cycle was 51.85 times of the one in the elastic range.

Fig. 20 shows the cumulative energy vs. cycles of the CT20-TH12-P model. Cumulative energy is the summation of dissipated energy through all the hysteresis cycles, where dissipated energy of each cycle has been calculated by obtaining the area under force-displacement curve. It can be observed that average of the absorbed energy in the inelastic range is 126.6 times of the one on elastic range. In addition, vertical deformation and load capacity of the ring in inelastic region

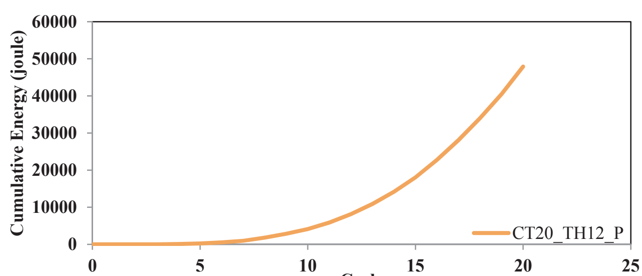

Fig. 20. Cumulative energy-loading cycle plot for CT20-TH12-P model.

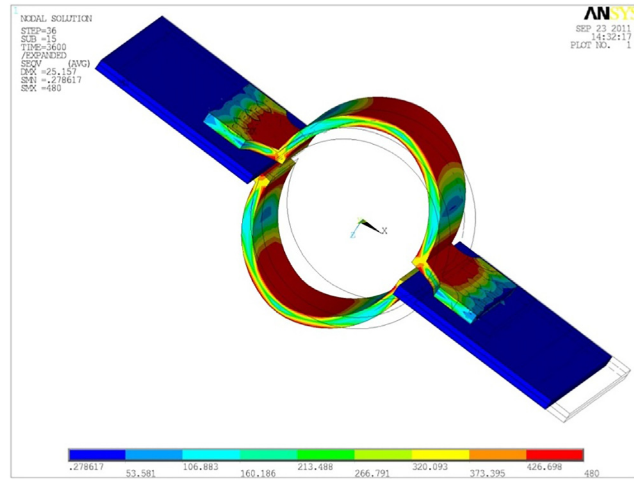

Fig. 21. Von Misses stress under cyclic load for CT20-TH12-P model.

were 9.48 and 1.87 times of the ones in elastic range, respectively. Fig. 21 shows Von Misses stress under cyclic load for CT20-TH12-P in ANSYS. It was observed that stress in the middle portion of this ring is higher in comparison with the previous model.

7.2. Steel ring made of 12 mm plate with CT20 steel and weld

In this section, same model that had been used in the previous section was simulated again while the bolts were replaced with fillet welds. CT20-TH12-SW is used for the model in this section as it represents the CT20 material, 12 mm thickness, and welding as the connector of the half rings. Hysteretic behavior of CT20-TH12-SW is presented in Fig. 22. Capacity of the model in tension and compression were around 135.9 kN and 113.6 kN, respectively.

Envelope of the hysteretic response of the model is shown in Fig. 23. Fig. 23 presents FEMA 356 two linearizations method [75], where the maximum vertical displacement and corresponding vertical displacement of the system at the end of the tensile elastic limit are 31.07 mm and 2.66 mm, respectively. Also, the same parameters under the compression force were 29.28 mm and 2.40 mm, respectively. Therefore, ductility of the CT20-TH12-SW model is:

$$\mu = \frac{\Delta_{Max}}{\Delta_y} = \frac{31.07}{2.66} = 11.68 \quad \text{Tension} \tag{15}$$

$$\mu = \frac{\Delta_{Max}}{\Delta_y} = \frac{29.28}{2.40} = 12.20 \quad \text{Compression} \tag{16}$$

Figs. 24 and 25 present the energy absorption vs. cycle and force vs. cycle of the model, respectively. It can be observed that inelastic capacity of the ring was 2.27 times of the one in elastic range. It was also

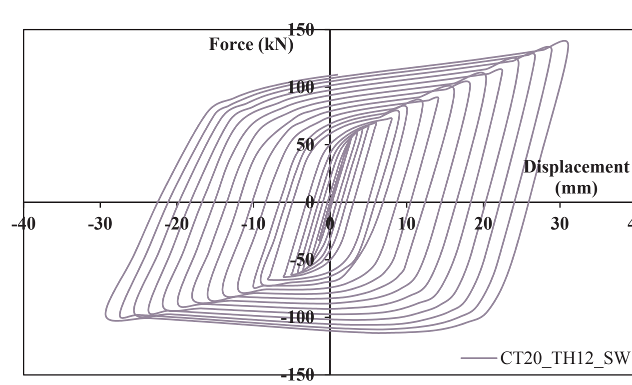

Fig. 22. Force-vertical displacement plot for CT20-TH12-SW model.

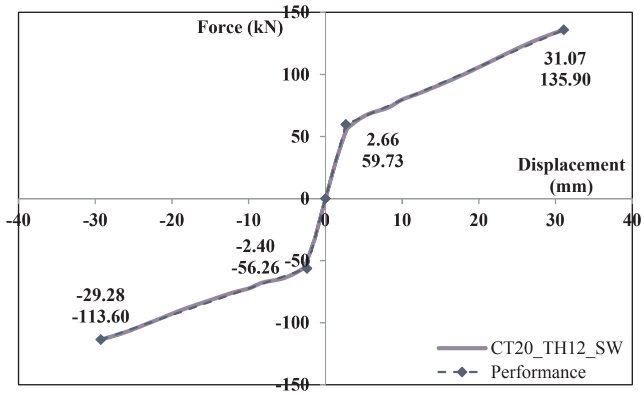

Fig. 23. Hysteresis loop push of force-displacement plot for CT20-TH12-SW model.

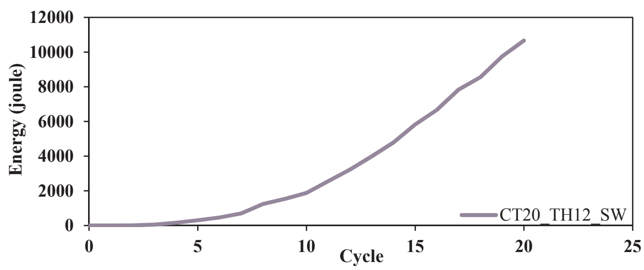

Fig. 24. Energy-loading cycle plot for CT20-TH12-SW model.

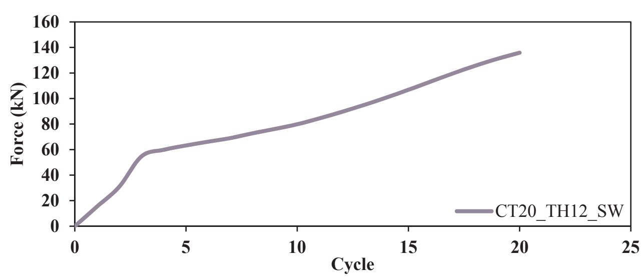

Fig. 25. Force-loading cycle plot for CT20-TH12-SW model.

concluded that peak dissipated energy in the inelastic range was 228 times of the one in elastic range. In other words, energy/force ratio in elastic range was 100.44 times of the ratio in elastic region.

Fig. 26 presents the cumulative energy vs. cycle in CT20-TH12-SW model. As can be seen in this figure, average of the dissipated energy in inelastic range was 242.62 times of the one in elastic range. It was also observed that peak displacement and load of the model in inelastic region were 10.68 and 2.27 times of the ones in elastic region. Fig. 27 shows Von Misses stress under cyclic load for CT20-TH12-SW in ANSYS. By comparing the Figs. 27 and 21, it can be concluded that utilizing bolts or welds does not have a significant effect on the stress

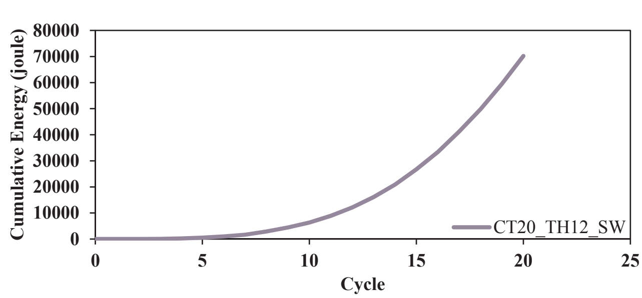

Fig. 26. Cumulative energy-loading cycle plot forCT20-TH12-SW model.

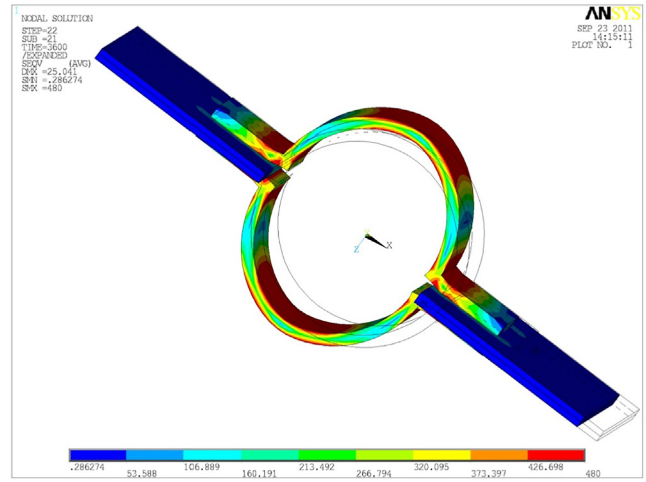

Fig. 27. Von Misses stress under cyclic load for CT20-TH12-SW model.

distribution in the ring.

7.3. Steel ring made of 12 mm plate with ST37 steel and weld

Similar model to CT20-TH12-SW was simulated in this section while ST37 was used as the material properties. ST37-TH12-SW was used as the name of this model representing ST37 as material, 12 mm thickness, and fillet weld for the connector of the half-rings. Hysteretic behavior of the model is shown in Fig. 28. The tension and compression inelastic capacity of the model were around 96 and 81 times of the elastic one, respectively.

Envelope of the hysteretic behavior of the ST37-TH12-SW is presented in Fig. 29. As presented in this figure, the maximum vertical displacement and corresponding vertical displacement of the system at the end of the tensile elastic limit are 24.00 mm and 3.26 mm, respectively, while similar parameters under the compression force were 24.00 mm and 3.23 mm, respectively, based on two linearizations method of FEMA 356 [75]. Ductility of ST37-TH12-SW can be calculated as follows:

$$\mu = \frac{\Delta_{Max}}{\Delta_y} = \frac{24.00}{3.26} = 7.36 \quad \text{Tension} \tag{17}$$

$$\mu = \frac{\Delta_{Max}}{\Delta_y} = \frac{24.00}{3.23} = 7.41 \quad \text{Compression} \tag{18}$$

Figs. 30 and 31 show the dissipated energy vs. cycle and load vs. cycle of ST37-TH12-SW model. It was observed that inelastic to elastic capacity of the model was around 1.28. In addition, it was concluded that dissipated energy in the inelastic range was around 80 times more

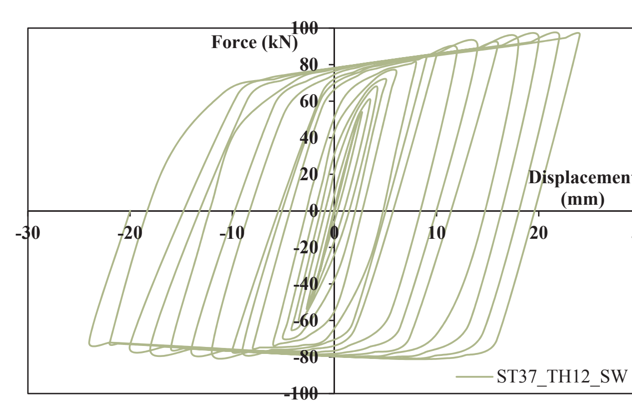

Fig. 28. Force-vertical displacement plot for ST37-TH12-SW model.

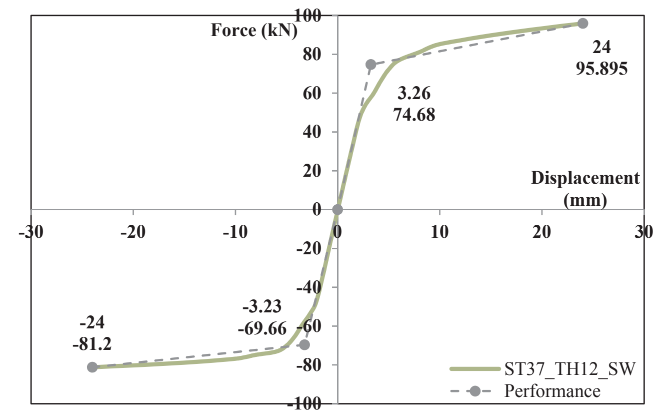

Fig. 29. Hysteresis loop push of force-displacement plot for ST37-TH12-SW model.

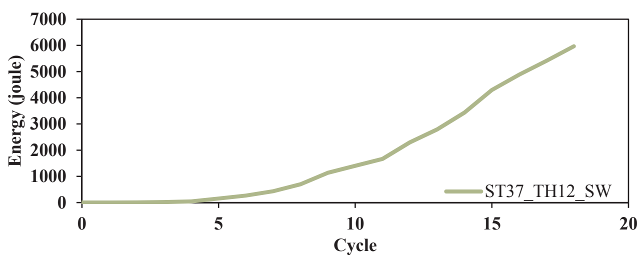

Fig. 30. Energy-loading cycle plot for ST37-TH12-SW model.

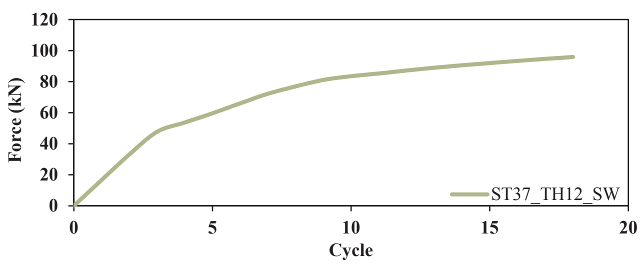

Fig. 31. Force-loading cycle plot for ST37-TH12-SW model.

than the one in elastic region. Therefore, energy/force in the inelastic region was 62 times of the one in elastic range.

Fig. 32 presents the cumulative energy vs. cycle in this model. As can be seen in this figure, average of the dissipated energy in the inelastic region was 46.6 times of the one in the elastic range. It was also noticed that peak displacement and force in the inelastic region were 6.36 and 1.28 times more than the ones in elastic range. Fig. 33 shows Von Misses stress under cyclic load for numerical model ST37-TH12-SW in ANSYS. As it was expected, by comparing Figs. 33 and 27, it can be observed that by reducing the material strength, stress intensity in the models increases and severer deformation is applied to the model.

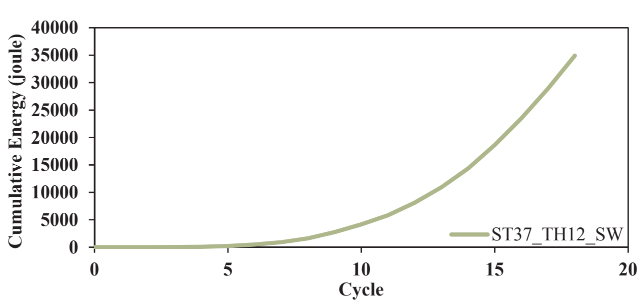

Fig. 32. Cumulative energy-loading cycle plot for ST37-TH12-SW model.

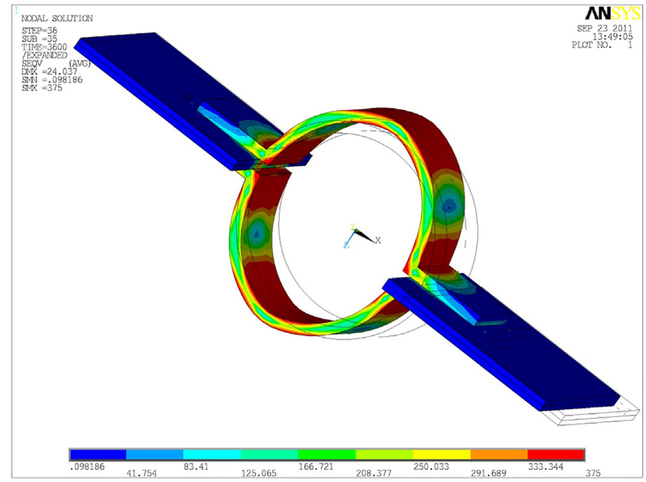

Fig. 33. Von Misses stress under cyclic load for ST37-TH12-SW model.

7.4. Steel ring made of 20 mm plate with ST37 steel and weld

Thickness of the steel ring under study is increased to 20 mm in this section. Model name ST37-TH20-SW was used for the simulation of this section. This name represents the ST37 steel as the material, 20 mm thickness, and fillet welding as the connector of the steel half-rings. Hysteretic behavior of this model is presented in Fig. 34. Tension and compression capacity of the model in inelastic range was 240.4 kN and 219.7 kN, respectively.

Envelope of the hysteretic behavior of the ST37-TH20-SW model is presented in Fig. 35, where the maximum vertical displacement and corresponding vertical displacement of the system at the end of the tensile elastic limit are 19.97 mm and 2.31 mm, respectively, according to propose two linearizations method by FEMA 356 [75]. Moreover, above mentioned parameters were 19.97 mm and 2.30 mm, respectively, following similar procedure under the compression force. Therefore, ductility of the model can be calculated as follows:

$$\mu = \frac{\Delta_{Max}}{\Delta_y} = \frac{19.97}{2.31} = 8.64 \quad \text{Tension} \tag{19}$$

$$\mu = \frac{\Delta_{Max}}{\Delta_y} = \frac{19.97}{2.30} = 8.68 \quad \text{Compression} \tag{20}$$

Figs. 36 and 37 show the dissipated energy vs. cycle and load vs cycle of the ST37-TH12-SW model, respectively. It was be observed that inelastic capacity of the model was 1.11 times of the elastic one. It was also concluded that inelastic dissipated energy and load in this model were 35.68 and 32.16 times of the elastic ones, respectively.

Cumulative energy of this model is demonstrated in Fig. 38. It was observed that the dissipated energy in the inelastic range to the elastic

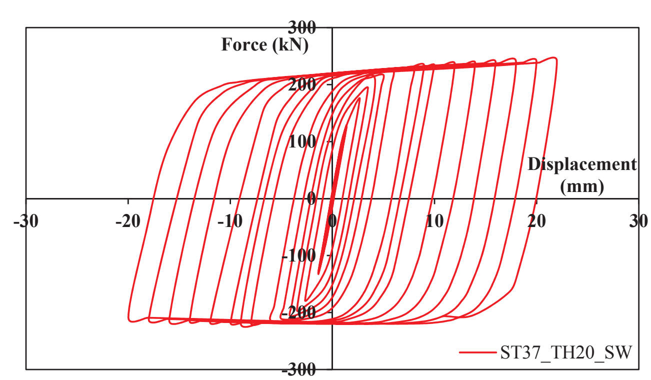

Fig. 34. Force-vertical displacement plot for ST37-TH20-SW model.

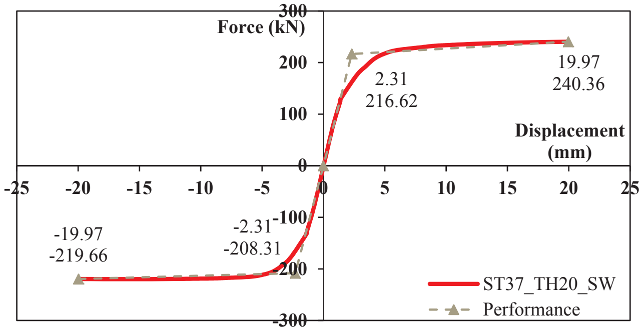

Fig. 35. Hysteresis loop push of force-displacement plot for ST37-TH20-SW model.

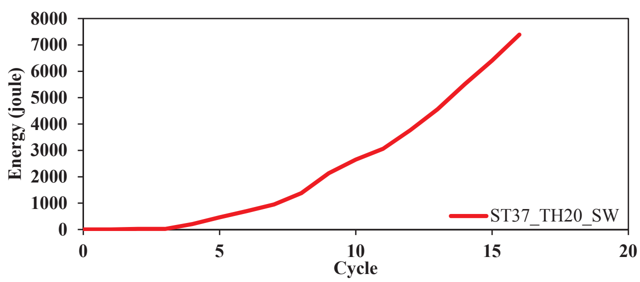

Fig. 36. Energy-loading cycle plot for ST37-TH20-SW model.

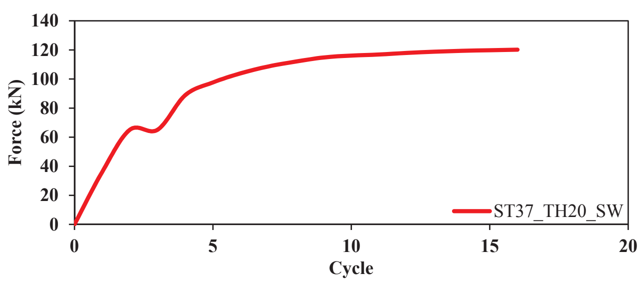

Fig. 37. Force-loading cycle plot for ST37-TH20-SW model.

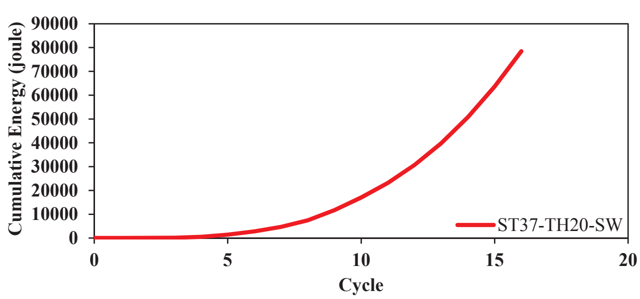

Fig. 38. Cumulative energy-loading cycle plot for ST37-TH20-SW model.

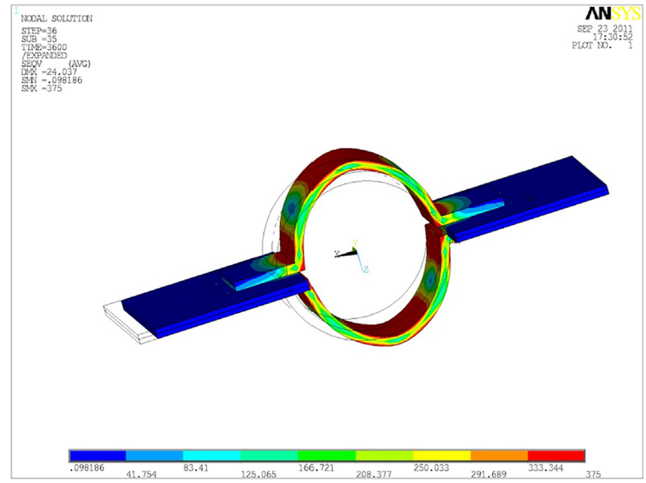

Fig. 39. Von Misses stress under cyclic load for ST37-TH20-SW model.

Table 2
Comparison between the ductility of all models.

Model type	Ductility	
	Tension	Compression
CT20-TH12-C	7.23	6.45
CT20-TH12-P	10.5	9.75
CT20-TH12-SW	11.68	12.20
ST37-TH12-SW	7.36	7.41
ST37-TH20-SW	8.64	8.68

one was around 51. In addition, inelastic vertical displacement and load bearing capacity of the model were 7.64 and 1.11 times of the ones in elastic range. Fig. 39 shows Von Misses stress under cyclic load for numerical model ST37-TH20-SW in ANSYS. It was observed that increasing the thickness of the steel ring effectively reduces the stress intensity of the model.

8. Comparison of the results

Comparison between the ductility of the all models presented in table 2. According to these results, CT20-TH12-SW has the most ductility factor compare to the rest of models, which was expected. To specify analytical results, the results of investigation on the loading cycles are shown in table 3. Based on displacement-loading cycle plots and cumulative energy-loading cycle plots the obtained results of presented models are shown in table 4. However, there are still other comparison to be considered, such that:

8.1. Effect of the material properties-comparison of CT20-TH12-SW and ST37-TH12-SW

Effect of the material properties on the performance of the steel rings is investigated in this section. For this purpose, response of the CT20-TH12-SW and ST37-TH12-SW cases are compared with each other. Comparison of the hysteretic behavior of two aforementioned models are presented in Fig. 40. As can be observed in this figure, maximum tensile force in the CT20 and ST37 cases were 19.64 kN and 95.89 kN, respectively. It was also observed that the peak compressive force in these models were 93.23 kN for CT20 and 81.2 kN for ST37 case. Therefore, tensile capacity of the ST37 case is about 20% less than the one in CT20 case. This reduction reduces to 13% under compression force.

Envelope curves of the hysteretic behavior of the two models are presented in Fig. 41. As can be seen in this figure, ductility of the CT20 case under tension force was 11.68, while it was 7.36 for ST37 case. Therefore, ST37 was 37% less ductile than CT20 case. On the other hand, ductility of CT20 and ST37 models under compression force were 12.2 and 7.4, respectively. It can be observed that ST37 model was 40% less ductile than CT20 case. It can be concluded that steel rings made of ST37 material are less ductile than the ones made of CT20. Table 5 presents the yielding force, initial stiffness and secondary stiffness of the models under tensions and compression. The comparison columns show the increase/decrease of the parameters of ST37 case in comparison to the CT20 one.

Energy and cumulative energy of the models versus cycles are presented in Figs. 41 and 42, respectively. It can be observed that total

Table 3
Analytical results of models.

Models	$E_{P-\max}$ (Joule)	$E_{E-\max}$ (Joule)	$P_{P-\max}$ (kN)	$P_{E-\max}$ (kN)	$\frac{E_{P-\max}}{E_{E-\max}}$	$\frac{P_{P-\max}}{P_{E-\max}}$	$\frac{\left(\frac{E_P}{E_E}\right)_{\max}}{\left(\frac{P_P}{P_E}\right)_{\max}}$
CT20-TH12-C	5611.53	55.05	92.74	44.34	101.93	2.09	48.77
CT20-TH12-P	7408.70	76.40	108.30	57.90	96.97	1.87	51.85
CT20-TH12-SW	10663.51	46.77	135.90	59.73	227.99	2.27	100.44
ST37-TH12-SW	5967.77	154.29	95.90	74.68	79.91	1.28	62.23
ST37-TH20-SW	14778.87	414.22	240.36	216.62	35.68	1.11	32.16

$E_{P-\max}$: Energy value in the last nonlinear cycle.
$E_{E-\max}$: Energy value in the last linear cycle.
$P_{P-\max}$: Force value in the last nonlinear cycle.
$P_{E-\max}$: Force value in the last linear cycle.
$\frac{E_{P-\max}}{E_{E-\max}}$: The ratio of energy in the last nonlinear cycle to energy in the last linear cycle.
$\frac{P_{P-\max}}{P_{E-\max}}$: The ratio of force in the last nonlinear cycle to force in the last linear cycle.

Table 4
Analytical results obtained by force-energy and force-loading cycle plots.

Models	CT20-TH12-C	CT20-TH12-P	CT20-TH12-SW	ST37-TH12-SW	ST37-TH20-SW
$\Delta_{P-\max}$ (mm)	22.18	30.29	31.07	24.00	19.97
$\Delta_{E-\max}$ (mm)	2.8	2.89	2.66	3.26	2.31
$\sum_{i=1}^{n} E_i$ (Joule)	27150.45	47910.19	70209.96	34904.97	78436.12
$\sum_{i=1}^{m} E_i$ (Joule)	58.62	94.42	51.03	285.92	505.35
$\frac{(\Delta_{P-\max}-\Delta_{E-\max})}{\Delta_{E-\max}}$	6.92	9.48	10.68	6.36	7.64
$\overline{E}_p = \frac{(\sum_{i-1}^{n} E_i - \sum_{i-1}^{m} E_i)}{(n-m)}$ (Joule)	2083.99	2988.48	4126.99	2663.00	6494.23
$\overline{E}_E = \frac{\sum_{i=1}^{m} E_i}{m}$ (Joule)	19.54	23.61	17.01	57.18	126.33
$\frac{\overline{E}_P}{\overline{E}_E}$	106.65	126.60	242.62	46.57	51.4

$\Delta_{P-\max}$: Lateral displacement of frame in the last nonlinear cycle.
$\Delta_{E-\max}$: Lateral displacement of frame in the last linear cycle.
$\sum_{i=1}^{m} E_i$: Total energy in "m" linear loading cycles.
$\sum_{i=1}^{n} E_i$: Total energy in "n" loading cycles.
$\frac{(\Delta_{P-\max}-\Delta_{E-\max})}{\Delta_{E-\max}}$: The ratio of nonlinear lateral displacement to Linear lateral displacement.
$\overline{E}_p = \frac{(\sum_{i=1}^{m} E_i - \sum_{i=1}^{n} E_i)}{(m-n)}$: Average energy per loading cycle in nonlinear limit zone.
$\overline{E}_E = \frac{\sum_{i=1}^{n} E_i}{n}$: Average energy per loading cycle in linear limit zone.
$\frac{\overline{E}_P}{\overline{E}_E}$: The ratio of average nonlinear energy to average linear energy per loading cycle.

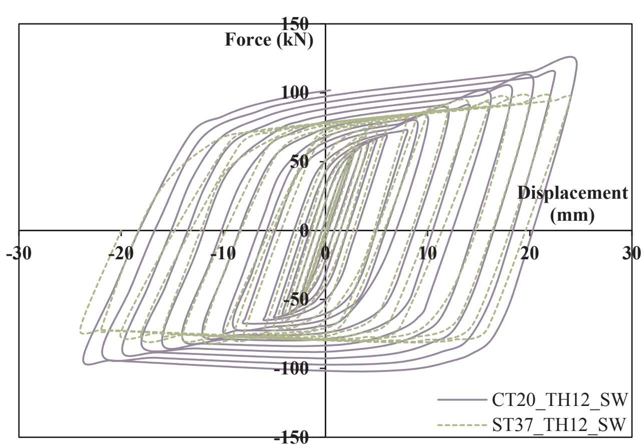

Fig. 40. Comparative hysteresis plots for CT20-TH12-SW and ST37-TH12-SW models.

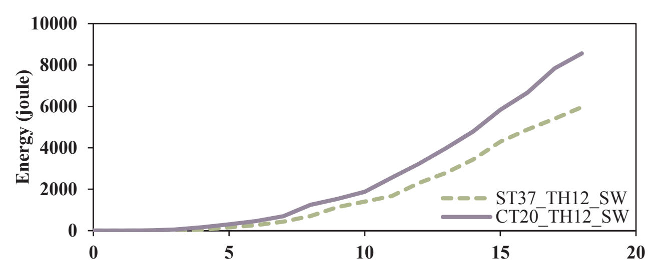

Fig. 41. Comparative energy-loading cycle plots for CT20-TH12-SW and ST37-TH12-SW models.

dissipated in ST37 and CT20 models were 34,905 and 49,793 Joule, respectively. Therefore, dissipated energy in CT20 model was 30% more than the one in ST37 case.

8.2. Effect of the thickness-comparison of ST37-TH12-SW and ST37-TH20-SW

In this section, effect of the thickness of the half-rings on the

Table 5
Comparison between CT20-TH12-SW and ST37-TH12-SW models.

Comparative results	Tension			Compression		
	ST37	CT20	Comparison (%)	ST37	CT20	Comparison (%)
Yielding force (kN)	74.68	59.73	+ 25.03	69.66	56.26	+ 23.82
Initial stiffness (kN/mm)	22.92	22.45	+ 2.09	21.56	22.51	-4.22
Secondary stiffness (kN/mm)	1.02	2.68	-61.94	0.55	2.13	-74.18

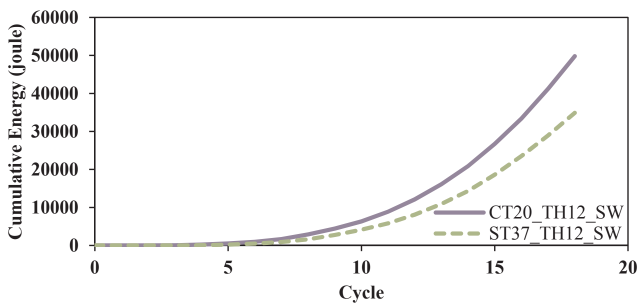

Fig. 42. Comparative cumulative energy-loading cycle plots for CT20-TH12-SW and ST37-TH12-SW models.

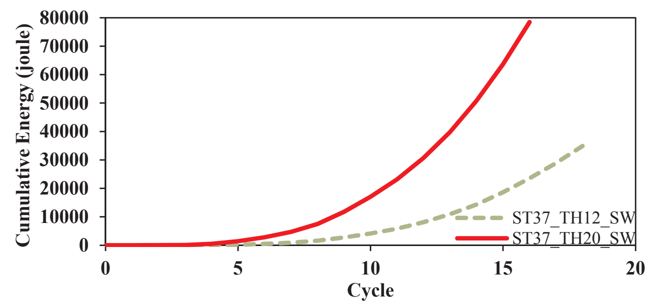

Fig. 45. Comparative cumulative energy-loading cycle plots for ST37-TH12-SW and ST37-TH20-SW models.

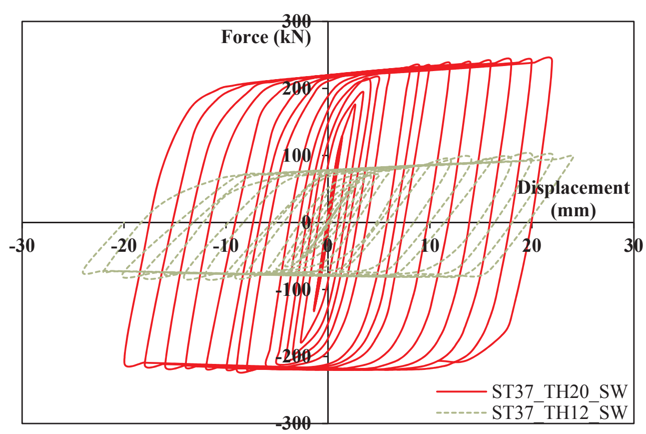

Fig. 43. Comparative hysteresis plots for ST37-TH12-SW and ST37-TH20-SW models.

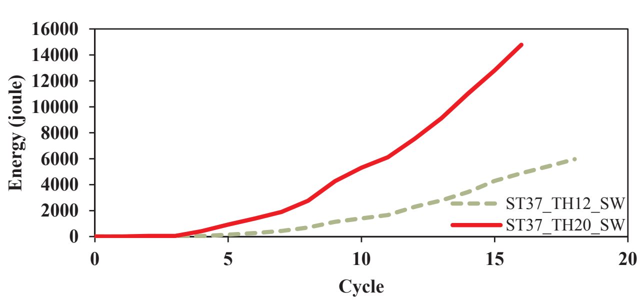

Fig. 44. Comparative energy-loading cycle plots for ST37-TH12-SW and ST37-TH20-SW models.

performance of the steel rings are evaluated. For this purpose, results of ST37-TH12-SW and ST37-TH20-SW models are compared with each other. Fig. 43 presents a comparison between the hysteretic responses of the models. As can be seen in this figure, tensile capacity of TH20 and TH12 cases were 241 kN and 96 kN, respectively. On the other hand, compressive capacity of the TH20 and TH12 models were 220 kN and 81.2 kN, respectively. Therefore, it can be concluded that tension and compression capacity of the TH20 model were 151% and 170.5% more than the ones in TH12 model.

Envelope curve of the hysteretic behavior of two models are presented in Fig. 44. As can be seen in this figure, ductility of models TH20 and TH12 under tension force were 8.64 and 7.36, respectively, and TH20 model was 17% more ductile than TH12 case. On the other hand, ductility of the model with 20 mm and 12 mm plates under compression force were around 7.4 and 8.7, respectively, meaning that TH20 model was 17% more ductile than TH12 case. Therefore, it can be concluded that thicker model was 17% more ductile than the other model. Table 6 presents the yielding force, initial stiffness and secondary stiffness of the models under tension and compression forces. The comparison columns show the increase/decrease of the specifications of the TH20 model in comparison to TH12 case.

Figs. 44 and 45 present the energy and cumulative energy of models versus loading cycles. The dissipated energy in the TH20 and TH12 models were 78,436 and 34,905 Joule. Therefore, energy dissipation in the TH20 model was 125% more than the one in TH12 case.

9. Conclusions

In this paper, ductility and energy dissipation capability of the steel rings constructed from two half-rings was investigated. Effect of the material properties and thickness of the half-rings on the performance

Table 6
Comparison between ST37-TH12-SW and ST37-TH20-SW models.

Comparative results	Tension			Compression		
	TH20	TH12	Comparison (%)	TH20	TH12	Comparison (%)
Yielding force (kN)	216.6	74.7	+ 190.0	208.3	69.7	+ 19
Initial stiffness (kN/mm)	93.4	22.9	+ 307.4	90.6	21.6	+ 320
Secondary stiffness (kN/mm)	1.34	1.02	+ 31.4	0.6	0.6	+ 16.4

of the steel rings was evaluated through finite-element simulations. This study concludes that:

(1) Steel rings made of two half-rings successfully dissipate the energy through inelastic behavior of the rings and they possess a significant ductility.
(2) Utilizing CT20 material instead of ST37 steel results in a significant increase in the load bearing capacity of the steel rings. It was also observed that ductility of CT20 model can be up to 40% larger than the one in ST37 model. Moreover, it was concluded that CT20 model was advantageous in terms of energy dissipation as well.
(3) Using a thicker steel ring significantly increases the capacity of the system and it also results in larger ductility of the model. In addition, incorporating thicker steel rings results in a considerable energy dissipation.
(4) Performance of steel rings made of two half-rings can be as effective as the ones made of a steel pipe. However, by using two half-rings, limitations on the size and thickness of the steel pipes will be overcome.

Appendix A. Supplementary material

Supplementary data associated with this article can be found, in the online version, at http://dx.doi.org/10.1016/j.engstruct.2018.05.034.

References

[1] Jin J, El-Tawil S. Seismic performance of steel frames with reduced beam section connections. J Constr Steel Res 2005;61(4):453–71.
[2] Itani A, Cheng Z, Saiidi M. Cyclic response of steel moment connections for large beam sections using haunch and reduced beam section concepts. Int J Steel Struct 2004;4(3):147–55.
[3] Kazemi MT, Momenzadeh S, Hoseinzadehasl M. Study of reduced beam section connections with web opening. In: 15th world conference on earthquake engineering, Lisbon, September; 2012.
[4] Momenzadeh S, Kazemi MT, Asl MH. Seismic performance of reduced web section moment connections. Int J Steel Struct 2017;17(2):413–25.
[5] Momenzadeh SB. Performance of circular opening in beam web connections. Life Sci J 2012;9(3):1377–83.
[6] Shariati M, et al. Experimental investigations on monotonic and cyclic behavior of steel pallet rack connections. Eng Fail Anal 2018;85:149–66.
[7] Murthy K, Application of visco-hyperelastic devices in structural response control. Civil and Environmental Engineering. Blacksburg, VA; 2005. MS Thesis, Virginia Polytechnic Institute and State University. MS.
[8] Code IS. Iranian code of practice for seismic resistant design of buildings [Standard No.2800, 3th ed.], Standard: Tehran, Iran; 2007.
[9] Shen J, et al. Seismic performance of concentrically braced frames with and without brace buckling. Eng Struct 2017;141:461–81.
[10] Momenzadeh S, Seker O, Shen J. Observed seismic demand on columns in SCBFs. In: AEI; 2017. p. 647–58.
[11] Momenzadeh S, Seker O, Faytarouni M, Shen J. Seismic performance of all-steel buckling-controlled braces with various cross-sections. J Constr Steel Res 2017.
[12] Ghods S, et al. Nonlinear behavior of connections in RCS frames with bracing and steel plate shear wall. Steel Compos Struct 2016;22(4):915–35.
[13] Hadianfard MA, Khakzad AR. Inelastic buckling and post-buckling behavior of gusset plate connections. Steel Compos Struct 2016;22(2):411–27.
[14] Serror MH, Abdelmoneam MN. Seismic performance evaluation of Egyptian code-designed steel moment resisting frames. HBRC J 2016.
[15] Jamkhaneh ME, Kafi MA. Experimental and numerical investigation of octagonal partially encased composite columns subject to axial and torsion moment loading. Civ Eng J 2017;3(10):939–55.
[16] Güneyisi EM, Gültekin A. Nonlinear behaviour of mid-rise steel buildings with gate braced frames. Open Civ Eng J 2017;11(1).
[17] Zahrai SM, Cheraghi A. Improving cyclic behavior of multi-level pipe damper using infill or slit diaphragm inside inner pipe. Struct Eng Mech 2017;64(2):195–204.
[18] Cheraghi A, Zahrai SM. Cyclic testing of multilevel pipe in pipe damper. J Earthquake Eng 2017:1–24.
[19] Zahrai SM, Cheraghi A. Reducing seismic vibrations of typical steel buildings using new multi-level yielding pipe damper. Int J Steel Struct 2017;17(3):983–98.
[20] Cheraghi A, Zahrai SM. Innovative multi-level control with concentric pipes along brace to reduce seismic response of steel frames. J Constr Steel Res 2016;127:120–35.
[21] Li W, Yang K, Wu L, Yu X, Chen L. Numerical study on composite ccstrcs frame structures under cyclic loading. J Struct Eng 2018;44:637–48.
[22] Wei Xing, Shariati M, Zandi Y, Pei Shiling, Jin Zhibin, Gharachurlu S, et al. Distribution of shear force in perforated shear connectors. Steel Compos Struct 2018;27(3):389–99.
[23] EbadiJamkhaneh M, Homaioon Ebrahimi A, Shokri Amiri M. Seismic performance of steel-braced frames with an all-steel buckling restrained brace. Pract Period Struct Des Constr 2018;23(3):04018016.
[24] Ebadi Jamkhaneh M, Kafi MA. Equalizing octagonal pec columns with steel columns: experimental and theoretical study. Pract Period Struct Des Constr 2018;23(3):04018012.
[25] Roufegarinejad A, Sabouri S. Nonlinear behavior of yielding damped bracing frames. In: 15th ASCE engineering mechanics conference, Columbia University, New York; 2002.
[26] Chen C, Lu L. Development and experimental investigation of a ductile CBF system. In: Proceedings of the 4th national conference on earthquake engineering; 1990.
[27] Thomopoulos K, Koltsakis E. Connections of CHS concrete-filled diagonals of X-bracings. J Constr Steel Res 2003;59(6):665–78.
[28] Deihim M, Kafi MA. A parametric study into the new design of a steel energy-absorbing connection. Eng Struct 2017;145:22–33.
[29] Abdi H, et al. Evaluation of response modification factor for steel structures with soft story retrofitted by viscous damper device. Adv Struct Eng 2016;19(8):1275–88.
[30] Abdi H, et al. Response modification factor for steel structure equipped with viscous damper device. Int J Steel Struct 2015;15(3):605–22.
[31] Ge H, et al. Experimental study on seismic performance of partial penetration welded steel beam–column connections with different fillet radii. Steel Compos Struct 2014;17(6):851–65.
[32] Shariati M, et al. Fatigue energy dissipation and failure analysis of angle shear connectors embedded in high strength concrete. Eng Fail Anal 2014;41:124–34.
[33] Shariati A, et al. Experimental assessment of angle shear connectors under monotonic and fully reversed cyclic loading in high strength concrete. Constr Build Mater 2014;52:276–83.
[34] Kachooee A, Kafi MA. A suggested method for improving post buckling behavior of concentric braces based on experimental and numerical studies. In: Structures. Elsevier; 2018.
[35] Kachooee A, Kafi MA, Gerami M. The effect of local fuse on behavior of concentrically braced frame by a numerical study. Civil Eng J 2018;4(3):655–67.
[36] Shafieifar M, Farzad M, Azizinamini A. Experimental and numerical study on mechanical properties of Ultra High Performance Concrete (UHPC). Constr Build Mater 2017;156:402–11.
[37] Shafieifar M, Azizinamini A, Director A. Alternative ABC connections utilizing UHPC; 2016.
[38] Farzad M, et al. Development of innovative bridge systems utilizing steel-concrete-steel sandwich. System 2017.
[39] Marshall JD, Charney FA. A hybrid passive control device for steel structures, I: Development and analysis. J Constr Steel Res 2010;66(10):1278–86.
[40] Marshall JD, Charney FA. A hybrid passive control device for steel structures, II: Physical testing. J Constr Steel Res 2010;66(10):1287–94.
[41] Mansouri I, et al. Strength prediction of rotary brace damper using MLR and MARS. Struct Eng Mech 2016;60(3):471–88.
[42] Boadi-Danquah E, MacLachlan D, Fadden M. Cyclic performance of a lightweight rapidly constructible and reconfigurable modular steel floor diaphragm. In: Key engineering materials. Trans Tech Publ; 2018.
[43] Kodur V, et al. Residual mechanical properties of high strength steel bolts subjected to heating-cooling cycle. J Constr Steel Res 2017;131:122–31.
[44] Eslami1a M, Namba H. Rotation capacity of composite beam connected to RHS column, experimental test results. Steel Compos Struct 2016;22(1):141–59.
[45] Eslami M, Namba H. Elasto-plastic behavior of composite beam connected to RHS column, experimental test results. Int J Steel Struct 2016;16(3):901–12.
[46] Eslami M, Namba H. Mechanism of elasto-plastic behavior of composite beam connected to RHS column. Int J Steel Struct 2016;16(3):913–33.
[47] Moghaddam HA, Estekanchi H. On the characteristics of an off-centre bracing system. J Constr Steel Res 1995;35(3):361–76.
[48] Moghaddam HA, Estekanchi HE. Seismic behaviour of offcentre bracing systems. J Constr Steel Res 1999;51(2):177–96.
[49] Zamani SM, Rasouli M. Experimental investigation of behavior of Y-shaped concentric steel bracing. Asian J Civ Eng (Build Housing) 2006;7(1):81–94.
[50] Zamani SM, et al. Experimental investigation of steel frames braced with symmetrical pairs of y-shaped concentric bracings. Int J Steel Struct 2011;11(2):117–31.
[51] Hosseini Hashemi B, Moaddab E. Experimental study of a hybrid structural damper for multi-seismic levels. In: Proceedings of the institution of civil engineers-structures and buildings; 2017. p. 1–13.
[52] Boostani M, Rezaifar O, Gholhaki M. Introduction and seismic performance investigation of the proposed lateral bracing system called “OGrid”. Arch Civ Mech Eng 2018;18(4):1024–41.
[53] Ibrahim YE, Marshall J, Charney FA. A visco-plastic device for seismic protection of structures. J Constr Steel Res 2007;63(11):1515–28.
[54] Chan RW, Albermani F. Experimental study of steel slit damper for passive energy dissipation. Eng Struct 2008;30(4):1058–66.
[55] Andalib Z, Kafi MA, Bazzaz M. Using hyper elastic material for increasing ductility of bracing. In: 1st conference of steel & structures and 2nd conference on application of high-strength steels in structural industry. Steel & Structures; 2010.
[56] Saunders RA. Nonlinear dynamic analysis of structures with hyperelastic devices. Virginia Tech; 2004.
[57] Abbasnia R, et al. Experimental and analytical investigation on the steel ring ductility. Sharif J Sci Technol 2008;52:41–8.
[58] Andalib Z, et al. Experimental investigation of the ductility and performance of steel rings constructed from plates. J Constr Steel Res 2014;103:77–88.
[59] Bazzaz M, et al. Evaluating the performance of OBS-C-O in steel frames under monotonic load. Earthquakes Struct 2015;8(3):697–710.

[60] Bazzaz M, et al. Numerical comparison of the seismic performance of steel rings in off-centre bracing system and diagonal bracing system. Steel Compos Struct 2015;19(4):917–37.
[61] Bazzaz M, et al. Evaluating the seismic performance of off-centre bracing system with circular element in optimum place. Int J Steel Struct 2014;14(2):293–304.
[62] Bazzaz M, et al. Evaluating the performance of steel ring in special bracing frame. In: 6th seismology and earthquake engineering international conf. Ministry of Science, Research and Technology; 2011.
[63] Bazzaz M, et al. Evaluation of the seismic performance of off-centre bracing system with ductile element in steel frames. Steel Compos Struct 2012;12(5):445–64.
[64] Bazzaz M, et al. Seismic behavior of off-centre bracing frame. In: 6th National congress on civil engineering; 2011.
[65] Andalib Z, et al. Investigation on the ductility and absorption of energy of steel ring in concentric braces. In: 2nd tructures. Steel and Structures; 2011.
[66] Bazzaz M. Seismic behavior of off-centre braced frame with circular element in steel frame design. Semnan University; 2010.
[67] Bazzaz M, et al. Modeling and analysis of steel ring devised in off-centric braced frame with the goal of improving ductility of bracing systems. Tehran (Iran): Iran Scientific and Industrial Researches Organization; 2012.
[68] Andalib Z. Experimental and numerical investigation on the ductility of steel ring constructed from steel plates in concentric braces. Semnan University; 2011.
[69] Escamilla E, Ostadalimakhmalbaf M. Capacity building for sustainable workforce in the construction industry. Prof Constr 2016;41(1):51–71.
[70] Khanzadi M, et al. Selecting the best strategy of labour productivity improvement in Tehran grade 1–3 construction contractor companies by applying analytic hierarchy process and statistical analysis of effective factors on labour productivity. In: The International symposium on the analytic hierarchy process (ISAHP), sorrento (Naples); 2011.
[71] Escamilla E, Ostadalimakhmalbaf M, Bigelow BF. Factors impacting Hispanic high school students and how to best reach them for the careers in the construction industry. Int J Constr Educ Res 2016;12(2):82–98.
[72] Southwell R. Castigliano's principle of minimum strain-energy. Proc Roy Soc Lond Ser A Math Phys Sci 1936;154(881):4–21.
[73] Roark RJ, Young WC. Formulas for stress and strain. McGraw-Hill; 1975.
[74] ATC. Guidelines for cyclic seismic testing of components of steel structures. ATC-24, Redwood City (CA); 1992.
[75] Council, BSS. Prestandard and commentary for the seismic rehabilitation of buildings. Report FEMA-356. Washington (DC); 2000.